Received: 26 December 2017 | Revised: 20 May 2018 | Accepted: 22 May 2018

DOI: 10.1002/cmr.b.21367

RESEARCH ARTICLE

WILEY

Slotted-waveguide array radio frequency coil for ultra-high-field magnetic resonance imaging

Milan M. Ilić[1,2] | Branislav M. Notaroš[1]

[1]Department of Electrical and Computer Engineering, Colorado State University, Fort Collins, CO, USA

[2]School of Electrical Engineering, University of Belgrade, Belgrade, Serbia

Correspondence
B.M. Notaroš, Department of Electrical and Computer Engineering, Colorado State University, Fort Collins, CO, USA.
Email: notaros@colostate.edu

Funding information
National Science Foundation, Grant/Award Number: ECCS-1307863; Serbian Ministry of Education, Science, and Technological Development, Grant/Award Number: TR-32005

Abstract

A novel radio frequency (RF) coil for ultra-high-field MRI in the form of a slotted waveguide array (SWGA) filled with a low-loss high-permittivity dielectric is proposed, evaluated, and demonstrated. A comprehensive computational electromagnetics study, along with basic RF measurements, to characterize the SWGA RF coil at 7T is presented. Slotted waveguides are robust structures capable of handling high powers. They are inherently narrow-band and have well defined linear polarization. When arranged in an array, they effectively generate high-quality B_1 field with strong B_1^+ and extremely low B_1^- and B_z components. With added dielectric lenses, the observed transmit efficiencies exceed 2.3 $\mu T\sqrt{W}$ in the human head model phantom, which is much higher than all results reported in literature. Moreover, we show that the proposed exciter, as an array with well-decoupled elements (measured isolation between elements is 33 dB or higher), can effectively be used for RF shimming. The novel coil generates RF magnetic field with excellent circular polarization, good uniformity, and negligible axial z-component, and it provides arbitrarily large or small field of view and excellent transmit efficiency, with and without dielectric lenses. It features well-defined narrowband operation, excellent isolation between ports/channels, and inherent possibilities for field optimizations via RF shimming and parallel imaging.

KEYWORDS

radio frequency coil, radio frequency shimming, slotted waveguide array, transmit efficiency, ultra-high-field magnetic resonance imaging

1 | INTRODUCTION

Generation and shaping of the radio frequency (RF) field, that is, design and engineering of the associated RF exciters (coils), has been an extremely active and rapidly growing field of research in magnetic resonance imaging (MRI). This is due to general tendencies to shift the imaging technology to higher static magnetic fields (B_0) in the everlasting strive to achieve better signal-to-noise ratio (SNR),[1] that can be traded for higher spatial resolution, as well as higher parallel imaging performances, allowing for higher acquisition acceleration factor. In ultra-high field (UHF) imagers ($B_0 \geq 7T$), the excitation wavelength becomes on the order of, or smaller than, the imaged sample. Hence, complex RF phase modulation and interference phenomena are readily observed in tissues at UHF, yielding undesired, highly nonuniform, RF magnetic field (B_1) distribution and low transmit efficiency.[2-7] Whole-body commercial imaging systems have been developed for 3T and researched in the form of transverse electromagnetic (TEM) coils up to 4T, with indications that they are feasible to 8T,[8] and demonstrated at 7T.[9] Among the novel, recently researched, RF exciters for UHF scanners that demonstrate commendable improvements in transmit efficiency and field homogeneity are the TEM "stripline" or dipole elements or loops, fed with multi-channel RF technology such

 © 2018 Wiley Periodicals, Inc.

as RF shimming and transmit SENSE.[10-17] We note here that the term "stripline", as used in[10] for instance, is actually inconsistent with the microwave terminology where the structure is firmly termed "microstrip". We will hence refer to this type of coil as a microstrip array as in ref. 18. Overall, RF coil design for human UHF scanners remains an area of intense development,[2,10,19,20] and especially regarding the most challenging targets, for example, those requiring torso RF excitation,[21-23] also known as body imaging.

This article proposes a novel method and coil for excitation of RF magnetic fields in UHF MRI systems using a slotted waveguide array (SWGA). The novel exciter provides RF magnetic field with excellent circular polarization (CP), that is, right-hand CP transverse field, $\mathbf{B}_1^+$, good field uniformity, high transmit efficiency, negligible axial z-component, arbitrarily large or small field of view (FOV), and inherent possibilities for field optimizations via RF shimming. Within these features, the SWGA coil has some clear advantages over existing RF exciters implemented in systems with static fields $B_0 \geq 7$T. In addition, each slotted waveguide antenna in the array is a mechanically robust structure capable of handling high powers. Each antenna is also a tuned resonator, with well-defined narrowband operation, and is well decoupled from all other elements in the array. At the same time, each antenna can be easily detuned (eg, for receiving operation) if needed. We note here that a slot-line antenna exciter suitable for parallel imaging has been reported in ref. 24. However, the exciter type, physics of RF field generation and radiation, as well as resulting antenna parameters and field patterns of a slot-line antenna are completely different than those of the slotted waveguide antenna used in this work.

The here-reported work proposes a novel idea and demonstrates the proof-of-concept of a SWGA RF coil for UHF MRI, with a focus on a 7T system. The article presents its design, characterization, and performance using computational electromagnetics (CEM) simulations, with the analysis based on a finite element method (FEM) code ANSYS HFSS.[25] This is a full-wave CEM technique that takes into account the geometry and material composition of the structure as is and includes all high-frequency, far-field effects, as well as all low-frequency, near-field effects, by numerically exactly solving the underlying Maxwell's equations and associated field boundary conditions.[26] It also presents basic RF measurements on a simple 3-element SWGA prototype, with an excellent measured isolation between the elements in the prototype. This enables very effective RF shimming, as shown via CEM simulations in the article, and provides a strong foundation for parallel imaging. MRI experiments with the SWGA coil at 7T are beyond the scope of this work and our experimental capability, and may be performed as part of our future work as a collaborative effort.

In terms of the transmit efficiency, for example, as one of the most critical characteristics and most significant challenges for UHF RF coil design, we show that the novel SWGA coil yields a much higher simulated efficiency than the state-of-the-art microstrip TEM array coil. Overall, the SWGA exciter proposed in this work yields higher transmit efficiencies than all those reported in the literature.

2 | METHODS

A single slotted waveguide antenna consists of a rectangular waveguide with slots milled into its conducting walls.[27] Depending on the desired polarization, the slots can be milled on either the broad or the narrow waveguide wall. In either case, the slots introduce discontinuities in the metallic waveguide structure, thus interrupting the flow of (surface) electric current in the waveguide walls. As a result, the electric charges accumulate along the edges of the slots, which are the source of the electric field across the slots, which, in turn, results in equivalent surface magnetic currents along the slots, and these currents radiate outside of the waveguide. From Babinet's principle[27,28] point of view, each slot represents a dipole-like magnetic-current antenna (with polarization orthogonal to that of the dual electric dipole). Moreover, because the slots are milled periodically along the waveguide, with each slot being fed by the wave inside the waveguide, the slotted waveguide antenna behaves like a linear uniform phased array of dipoles. To achieve desired polarization in the proposed application, we here consider a slotted waveguide antenna with slots in the narrow wall, as shown in Figure 1.

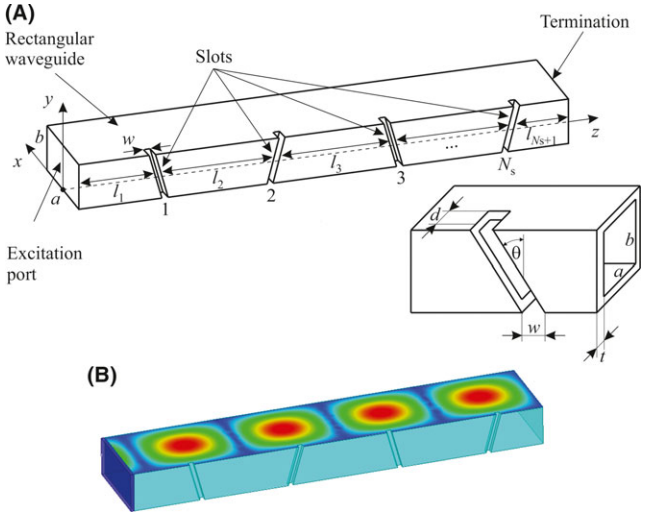

FIGURE 1 A, Slotted-waveguide antenna with N_s (four) slots milled in the narrow wall; B, Electric field distribution on the top waveguide wall

There are 2 basic types of slotted waveguide antennas: a standing-wave antenna and a traveling-wave antenna. In both cases, the antenna is fed at the excitation port and operates in the monomode (TE_{10}) regime.[26] However, in a standing-wave antenna, the waveguide is terminated with a short circuit (metallic plate), whereas the termination in a traveling-wave antenna is in the form of a matched load (absorber). Standing-wave slotted waveguide antennas, being a form of electromagnetic resonators, are inherently narrowband, which is a desired property in the proposed application, where RF excitation is required strictly at the Larmor frequency and the radiation in the broader spectrum is actually considered as a loss. In addition, they are easier to manufacture than the traveling-wave antennas. Although traveling-wave slotted waveguide antennas can also be used as RF exciters in MRI, for the reasons outlined above, in what follows we consider short-circuited standing-wave slotted-waveguide antennas.

Geometry of a slot is shown in Figure 1A in more detail. The inner width and height of the rectangular waveguide are a and b ($a > b$), respectfully, with the wall thickness being t. In the proposed application, t can be very small (eg, 17 μm or less) in order to minimize the induced eddy currents which may arise due to operation of the gradient coils, hence it is negligible for most purposes and thus it is most often not shown in the figures. With reference to Figure 1A, the slots are numbered starting from the excitation port on the left, toward the termination on the right. The number of slots N_s is generally arbitrary; it can be smaller or larger depending on the desired FOV. The distance between the excitation port and the first slot, l_1, distances between the slots, $l_2, l_3, \ldots, l_{N_s}$, and the distance between the last slot and the termination, l_{N_s+1}, can all be optimized for optimal radiation and impedance matching.[29] For appropriate operation, the distances between the slots are approximately $\lambda_g/2$ and, for the standing-wave array, the distance between the last slot and the short-circuited termination is about $\lambda_g/4$, where λ_g stands for the guided wavelength along the waveguide.[26] Distance l_1 varies based on the type of the waveguide feed, but it can be considered to be $\lambda_g/4$ as well. Shown in the right inset of Figure 1A is a detail of the geometry of a single slot. The slot is tilted at an angle θ from the vertical axis (to enable efficient disruption of the currents), its width is w, and its depth extending beyond the wall thickness is d. This is necessary to ensure efficient radiation, that is, a dipole-like behavior.

In order to enable a monomode, TE_{10}, operation, of the waveguide, its transversal width a of about $\lambda/2$, λ being the (unguided) wavelength in the medium occupying the waveguide. At very high frequencies, this wavelength is small enough and the dielectric in the waveguide can be air. On the other hand, in MRI applications at 7T, where Larmor frequency is about f = 300 MHz, this dimension is prohibitively large to enable practical waveguide design. However, the waveguide can be filled with a low-loss high-permittivity dielectric. For instance, a dielectric of water-like properties with relative permittivity $\varepsilon_r = 81$ and conductivity $\sigma = 0.0002$ S/m reduces the waveguide dimensions $\sqrt{\varepsilon_r} = 9$ times. In this case, a standard WR284 waveguide ($a = 72.136$ mm, $b = 34.036$ mm) can be used. Alternatively, a similar non-standard rectangular waveguide can be readily designed. In the given example, we have $\lambda_0 = c_0/f = 0.99931$ m, where λ_0 and c_0 are the free-space wavelength and the speed of light in a vacuum, respectively, and $\lambda = \lambda_0/\sqrt{\varepsilon_r} = 0.11103$ m. The cutoff frequency for the TE_{10} mode is computed as $f_c = c/(2a) = c_0/(2a\sqrt{\varepsilon_r}) = 230.87$ MHz. The cutoff frequency for the TM_{01} mode in this case is 489.281 MHz. This leaves a monomode window of operation from 230.87 to 489.28 MHz. Finally, the guided wavelength in this case is $\lambda_g = \lambda/\sqrt{1-(f_c/f)^2} = 173.88$ mm. At this point, we remark that allowing a higher cutoff frequency of the dominant mode, that is, pushing it closer to the operating frequency f, a dielectric of lower permittivity (most commonly associated with lower dielectric losses) can be used as a waveguide filler, while keeping the waveguide dimensions and other geometrical parameters the same. Furthermore, in the given example, referring to Figure 1A, we have $N_s = 4$, $l_1 = 53.634$ mm, $l_5 = \lambda_g/4 = 43.471$ mm, $l_2 = l_3 = L_4 = \lambda_g/2 = 86.942$ mm, $\theta = 15°$, and $t = 4$ mm. For a single-slotted waveguide (with parameters given above) in free space, the generated E-field (normalized complex magnitude) in the waveguide is shown in Figure 1B. It is clear from the figure that the slots reside in areas where the standing wave in the waveguide has its maxima; this ensures optimal radiation. If properly fed, the slotted-waveguide antenna has a well defined linearly polarized magnetic field oriented parallel to the waveguide narrow side (in the x-z plane). In addition, at distances of $a/2$ from the slotted side, z-component of magnetic field practically vanishes.

As a feeding structure for an array of slotted waveguides, a standard coaxial-line-to-rectangular-waveguide transition[26] is used. In the array, each of the waveguides is fed by a coaxial line with a small probe protruding into the rectangular waveguide. The probe is located approximately $l_f \approx \lambda_g/4$ from the short-circuited termination. Its height, diameter, and position can be optimized to obtain (as close as possible) desired feeding parameters (eg, input impedance) and for optimal excitation of the dominant TE_{10} mode. To simplify field analysis, the feeding probe is omitted in the models to follow and the waveguides are excited utilizing a standard TE_{10} mode excitation via a wave port.

We have built a simple 3-element SWGA prototype, shown in Figure 2A, with waveguides filled with water and slots sealed with 3-D printed ABS plastic, and have

performed RF measurements on this prototype in the Electromagnetics Laboratory. As one possibility for impedance matching of the elements to the nominal impedance of 50 Ω, Figure 2B shows a microstrip matching network comprising 3 variable trimmer capacitors with capacitances ranging from 8 pF to 40 pF.

Based on this preliminary analysis in Figure 1, we construct an array of N_a slotted waveguides, arranged as shown in Figures 3 and 4A, which constitutes a SWGA RF coil. This array, when excited with identical incident powers, appropriately phase shifted by $-2\pi/N_a$, produces, in air, a very uniform CP transverse (to z) RF magnetic field along the array axis (z-axis) and in its vicinity. The array generates a similar field when it is loaded with a subject and inserted in the MRI bore. When loaded, due to the subject's potentially high permittivity and inhomogeneity, the homogeneity of the CP field of the SWGA will be disrupted and degraded; however, it can be improved and optimally restored by adjusting the excitations (and/or positions) of the array elements in the process of RF shimming.[8,10,30-37]

To further improve the efficiency of the exciter, we propose adding a low-loss high-permittivity dielectric on each of the slotted waveguides, in front and surrounding the slotted-waveguide side. The role of the dielectric is to provide a sort of smoother impedance transition from slots into free space and reduce the backward radiation. In a sense, the dielectric performs as a basic lens, facilitating focusing of the radiation in the desired direction. Alternatively, a lens of an optimized shape and dielectric profile, or an array of lenses, can be utilized as well.

3 | RESULTS

In order to examine the SWGA operation in an MRI bore, we consider a metallic bore (shield) of radius r_b = 450 mm and length l_b = 1 m, placed coaxially with the array axis, with array centered in the bore. We next let $N_a = 16$, and set the radius of the array (distance from the z-axis to the middle of the waveguide cross section, as shown in Figure 3A) to $r_a = 200$ mm. Exciting each port with a "standard" excitation, that is, equal incident power at all ports and phase shifts of $-2\pi/16$ between the excitations of adjacent elements in the clockwise direction, we analyze the magnetic field inside the unloaded array. To enable TE_{10} excitation via wave-type ports, the waveguides are terminated at the ports with metallic plugs. With dimensions of the slots and their distances given above, the total length of the waveguides is $l_w = 360$ mm, as depicted in Figure 3D. No dielectric lenses are used. The results of this analysis are shown in Figure 3.

We then consider a homogeneous dielectric ($\varepsilon_r = 43.776$, $\sigma = 0.41335$ S/m) elliptic cylinder, acting as a simple phantom (resembling a human head). The long and short semi-axes of the ellipse are 10 cm and 8 cm, respectively, the cylinder is 24 cm long, and it is centered at the center of the array, as shown in Figure 4A. The SWGA coil and metallic (MRI) bore dimensions are as in the previous example (in Figure 3). Figure 4B,C show the simulation results for the transmit efficiency evaluated as $|\mathbf{B}_1^+|/\sqrt{P_a}[\mathrm{T}/\sqrt{\mathrm{W}}]$, where P_a is the total accepted power for the coil, and $|\mathbf{B}_1^-|$ field component, respectively, in the central (at the middle of the phantom) axial cross section of the phantom, with no dielectric lenses.

With all ports matched to ensure the return loss RL $\geq$ 20 dB, the computed transmission between the first element and the remaining elements of the array is between −42 dB and −27 dB, noting that similar relations exist for the remaining ports and their mutual transmissions (couplings).

Utilizing the designed microstrip matching network in Figure 2B on each of the 3 SWG elements in the 3-element SWGA prototype in Figure 2a, measured $|S_{11}|$, in free space, is lower than −36 dB. Two waveguides have also been placed next to each other, in open space, to simulate

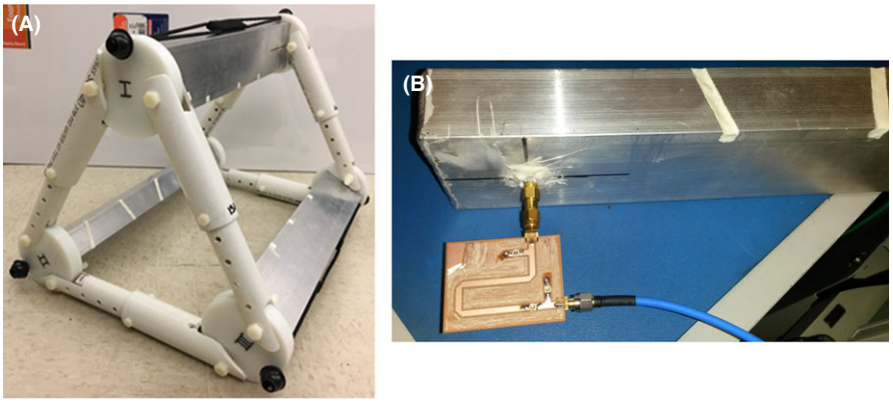

FIGURE 2 A, Simple 3-element SWGA RF coil prototype; B, Detail showing one slotted waveguide with the attached matching network

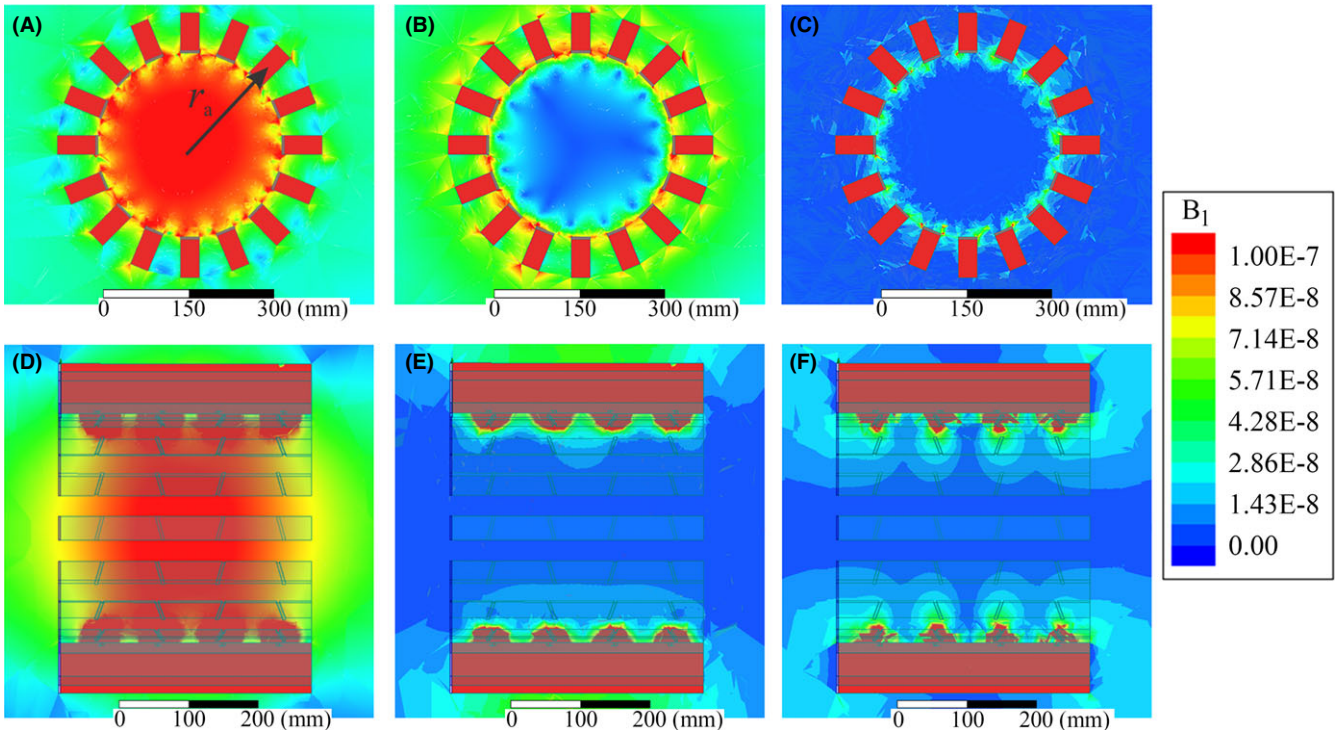

FIGURE 3 Complex magnitudes of the magnetic field components (in T) generated by the slotted-waveguide array (SWGA) RF coil in the 7T bore in air normalized for 1 W total accepted power, in the central (at the middle of the coil) axial (transversal) cross section A-C, and the sagittal cross section D-F: A, D $|\mathbf{B}_1^+|$ field component; B, E $|\mathbf{B}_1^-|$ field component; and C, F $|\mathbf{B}_z|$ field component

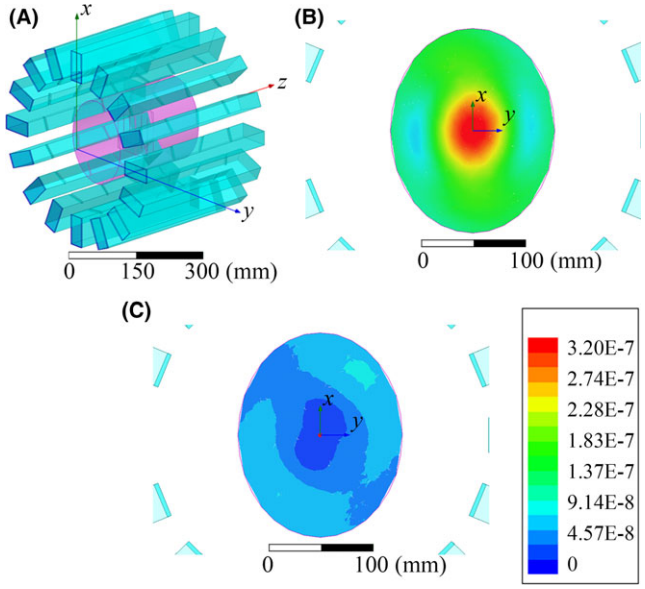

FIGURE 4 Simulation results for the phantom-loaded SWGA RF coil in the 7T bore with "standard" excitation: A, problem geometry, showing 16 slotted waveguides around an elliptic cylinder phantom (metallic bore is not shown), and B, transmit efficiency, $|\mathbf{B}_1^+|/\sqrt{P_a}[\mathrm{T}/\sqrt{\mathrm{W}}]$ (P_a is the total accepted power), and C, $|\mathbf{B}_1^-|$ [T] field component in the central axial cross section of the phantom

close proximity as if they were arranged in a 16-element array, in Figure 4A, and the measured transmission $|S_{21}|$ between them (coupling) is lower than −33 dB. The measured isolation is even higher between elements in the prototype in Figure 2A. Shown in Figure 5 is the reflection coefficient of a single-slotted waveguide element. The figure shows both simulated (in a bore) results and the worst case (of the 3 built prototypes) bench-measured results (in free space). Simulated and measured Q-factors are about 120 and at least 50, respectively.

Figure 6 shows comparison of efficiencies obtained by a 16-element microstrip TEM coil (similar to the one described in the ref. 10 with the elements forming a

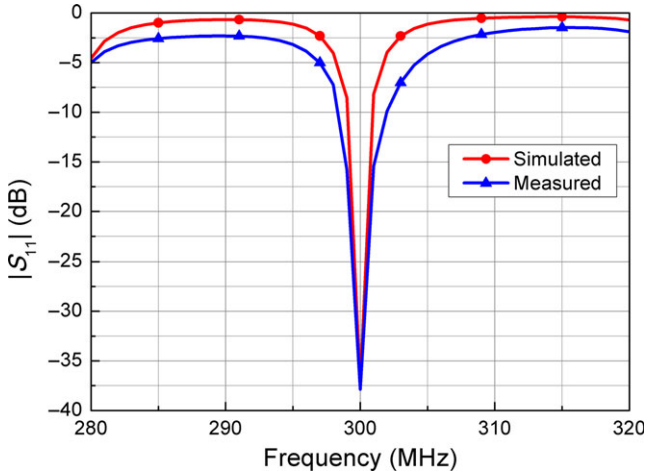

FIGURE 5 Simulated and measured reflection coefficient of a single matched slotted-waveguide element

circular array) and by the 16-element SWGA coil with dielectric lenses ($\varepsilon_r = 30$, $\tan\delta \approx 0$) in imaging of the saline ($\varepsilon_r = 82$, $\sigma = 0.6$ S/m) phantom having the same dimensions as in the example in Figure 4. The microstrip coil is described in detail in the context of the following example and is depicted in Figure 8 and the SWGA coil and bore dimensions are as in the examples in Figures 3 and 4. The color code in Figure 6A,B is adjusted to show the full span of obtained efficiencies in both cases. Note that the dielectric constant of the lens in our examples was chosen to be close to one half of the dielectric constant of the water and physically realizable using ethylene-glycol or titanium-oxide powders. However, it can be optimized to yield better performance.

As the next example, we consider a simple 12-tissue human head model 220 mm long from the tip of the nose to the back of the scull, as shown in Figure 7A. The head is positioned inside the SWGA as depicted in Figure 7B. The array also comprises an annulus—a hollow dielectric ($\varepsilon_r = 30$) cylinder (a lens) whose outer cylindrical surface covers the waveguide slots, as shown in Figure 7B,C. The bore, waveguides comprising the array, and their position in the bore are the same as in the previous examples in Figures 3, 4, and 6, with the exception of the array radius, which is set to $r_a = 230$ mm. The inner and outer radii of the dielectric lens are $r_{in} = 150$ mm and $r_{out} = 200$ mm, respectively. The height of the lens is $l_d = 350$ mm and it is placed symmetrically with respect to the array, as shown in Figure 7D.

To facilitate correct and as fair as possible comparison with one of the alternative highly efficient RF array coils, we again construct a model of a 16-element microstrip TEM circular array closely resembling the array utilized in ref. 10. The array with the head model is shown in Figure 8A and it is also positioned at the center of the metallic bore. Referring to Figure 8A-C, the height of the microstrip array is $l_s = l_w = 360$ mm, the radius (from the center of the array to the middle of the dielectric substrate) is $r_s = 200$ mm, and the widths of the outer and inner copper strips are $w_{os} = 60$ mm and $w_{is} = 12$ mm, respectively. The strips are considered to be infinitely thin. Feeding of the strips is as described in ref. 10, with the same phase shifts as applied to the SWGA ($-2\pi/16$ between the excitations of adjacent elements in the clockwise direction). The dielectric substrate carrying the strips is $h_s = 5$ mmthick Teflon (dielectric constant and loss tangent are $\varepsilon_r = 2.1$ and $\tan\delta = 0.001$, respectively).

With such defined human head model and the SWGA and microstrip TEM array coils, we investigate and discuss the efficiency of the 2 coils focusing on the axial cross section of the cranium and on the sagittal cross section of the

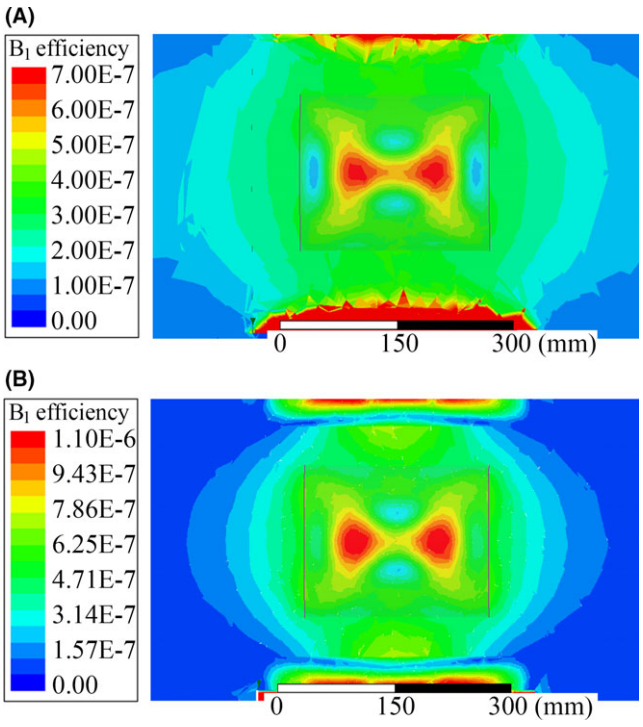

FIGURE 6 Comparison of computed efficiencies, $|\mathbf{B}_1^+|/\sqrt{P_a}[T/\sqrt{W}]$, at 7 T obtained by A, the microstrip TEM coil and B, the SWGA coil from Figure 4A with dielectric lenses (ε_r = 30 and negligible tanδ) added in front of the slotted-waveguide sides of all elements in the array. Note that the scales in A and B are different

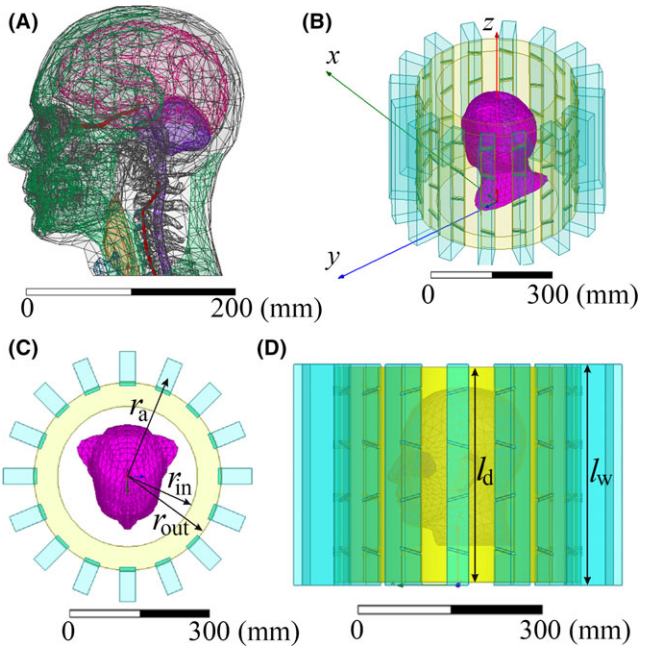

FIGURE 7 Analysis of a SWGA coil with a human head phantom model in the MRI bore at 7T: A, head model incorporating 12 tissues; B-D, 3 different views of the head model inside the SWGA coil from Figure 4 with a hollow dielectric cylinder lens, showing relative positions of the SWGA, lens, and phantom

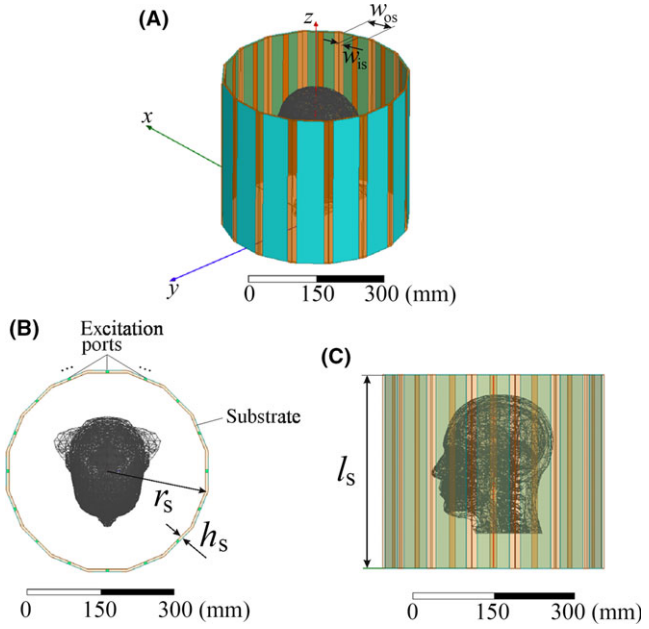

FIGURE 8 Analysis of the human head model from Figure 7A inside a 16-element microstrip TEM circular array coil closely resembling the array utilized in the ref. 10: A-C, 3 different views of the structure

head, Figure 9A-D. A symmetrically placed rectangular cut in the same axial cross section, depicted in Figure 9E, is later used for optimization of the field uniformity by RF shimming. The sides of the rectangular cut are $a_{cut} = 110$ mm and $b_{cut} = 140$ mm.

In Figure 9A,B, we present the simulated efficiency $|\mathbf{B}_1{}^+|/\sqrt{P_a}$ [T/$\sqrt{\text{W}}$] of the SWGA exciter from Figure 7. For comparison, in Figure 9C,D, we show the simulated efficiency of the microstrip TEM array from Figure 8. Comparison of the SWGA transmit efficiencies with several results found in the literature is given in Table 1. In addition, Figure 9F,G show the electric field (complex magnitude) distribution for the SWGA array and the microstrip array, respectively.

To demonstrate the possibility for RF shimming of the SWGA coil in this example, for the system in Figure 7, we use the rectangular cut in the axial cross section, shown in Figure 9E, in which we consider a rather coarse uniform grid of 21 × 21 points for explicit evaluation of the field. We first evaluate the efficiency for the "standard" (nominal) excitation and then optimize the excitations to minimize deviation of the efficiency in the established grid by running a genetic algorithm. The 31-dimensional optimization space comprises 16 excitation magnitudes, that is, incident powers, and 15 phases (arguments of the complex excitations). Note that the phase of one (eg, the first) excitation can be fixed to reduce the optimization space and prevent periodic solutions. This rough preliminary optimization yields a decrease of the standard deviation for the computed transmit efficiency from 0.48 $\mu\text{T}/\sqrt{\text{W}}$ to 0.31 $\mu\text{T}/\sqrt{\text{W}}$, with simultaneous decrease of its mean from 1.5 $\mu\text{T}/\sqrt{\text{W}}$ to 1.10 $\mu\text{T}/\sqrt{\text{W}}$. As a graphic representation of the RF shimming effect, we present in Figure 10 the magnitude of the efficiency gradient before and after optimization.

4 | DISCUSSION

We observe from Figure 3 that the air-filled SWGA RF coil with the "standard" excitation in the 7T bore produces highly homogeneous B_1^+, extremely low B_1^- (left-hand CP transverse field), and practically vanishing B_z (axial component of B) in the whole region encompassed by the array (except in the region very close to the antennas, which is irrelevant for imaging applications).

It can be seen from Figure 4B,C that the efficiency of the SWGA coil when loaded with a simple phantom in the form of a homogeneous dielectric elliptic cylinder peaks at the middle of the cross section at 0.32 $\mu\text{T}/\sqrt{\text{W}}$, as well as that very low $|\mathbf{B}_1{}^-|$ is maintained in the whole cross section.

In relation to the results in Figure 4, we can additionally conclude that the observed (computed) low coupling (excellent isolation) between elements in the phantom-loaded SWGA array (between −42 dB and −27 dB), with all ports well matched (RL ≥ 20 dB), provides a strong basis for both parallel imaging and effective RF shimming.

Based on RF measurements on simple SWGA prototypes, as in Figure 2, we have found that impedance matching of the slotted waveguides to 50 Ω is very simple to do. Utilizing simple matching networks, the SWGA impedances can be practically perfectly tuned. Furthermore, measured isolation between the elements in the prototypes is very high.

As can be seen from Figure 5, the 2 sets of reflection coefficient results, via simulations and bench measurements, are in a very good agreement. Lower measured Q-factor is primarily attributed to the fact that water in waveguides causes corrosion of the waveguide walls and aluminum particles dissolved in water introduce additional loss; we have also noticed the lowering of the measured Q-factor over time. Both problems can be solved in the future by coating the waveguide walls or using different low-loss dielectric (with similar dielectric constant, eg, based on titanium-oxide powers) inside the waveguide.

It can be seen from Figure 6A,B that both the 16-element microstrip TEM coil (as in the ref. 10) and the 16-element SWGA coil with dielectric lenses produce similar field distribution inside the saline phantom and outside of it. However, the SWGA array produces maximum

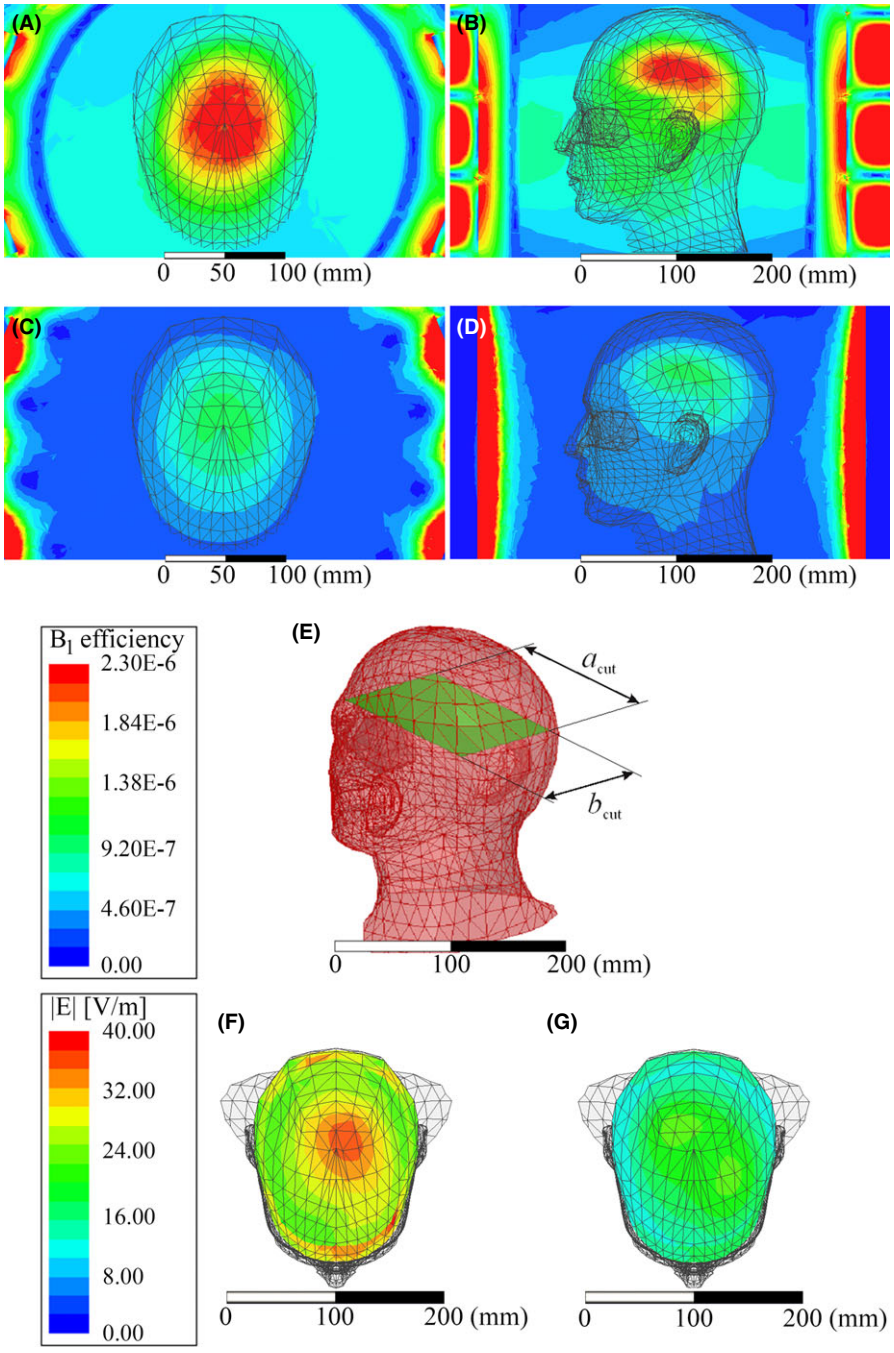

FIGURE 9 Simulated transmit efficiency, $|\mathbf{B}_1^+|/\sqrt{P_a}[\mathrm{T}/\sqrt{\mathrm{W}}]$, of (A, B) the SWGA/head model in Figure 7 and (C, D) the microstrip-array/head model in Figure 8, in the axial cross section of the head model A-C and the sagittal cross section of the model B-D. Rectangular cut, depicted in E, resides in the chosen axial cross section and is later used for analysis of RF shimming performance. Electric field (complex magnitudes) for 1 W accepted power in case of F, SWGA array and G, microstrip array

efficiency of about 1.1 $\mu\mathrm{T}/\sqrt{\mathrm{W}}$, whereas it is about 0.7 $\mu\mathrm{T}/\sqrt{\mathrm{W}}$ for the TEM array, yielding approximately 57% improvement obtained by the proposed exciter array. Note that the obtained efficiency is greater than all of those reported in.[30,31,38-40]

We observe based on the results in Figure 9 that the overall (magnetic) field distributions in both axial and sagittal cross sections of the 12-tissue human head model are practically the same for both arrays considered, the SWGA coil from Figure 7 and the microstrip TEM array coil from Figure 8 (as in the ref. 10). However, the efficiency of the SWGA exciter is much higher than that of the microstrip array. Namely, the peak efficiency obtained by the SWGA coil is 2.39 $\mu\mathrm{T}/\sqrt{\mathrm{W}}$, whereas for the TEM coil it is about 1.0 $\mu\mathrm{T}/\sqrt{\mathrm{W}}$. Thus, in this case, the SWGA coil provides 130% improvement in the (computed)

TABLE 1 Comparisons of SWGA transmit efficiencies with results from the literature

Reference	Coil type	Reported transmit efficiency [$\mu T/\sqrt{W}$]	Note	Reported transmit efficiency [$\mu T/\sqrt{W}$]	Note
This work	Slotted waveguide array	2.39	Peak Quadrature	1.74	Peak Shimmed
28	Coaxial waveguide	0.44	Head Quadrature	0.07	Head Shimmed
29	Coaxial waveguide	0.30	Cylindrical phantom	0.12	Head
36	Traveling wave array with rods	0.158	Peak		
37	TEM resonator	0.16	Peak		
38	Transmission line array	0.27			

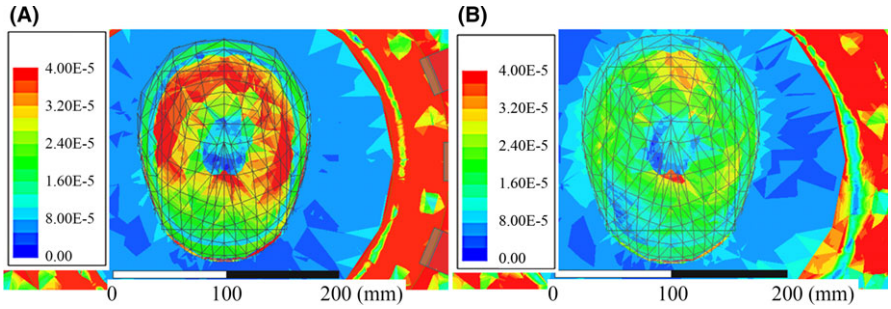

FIGURE 10 The magnitude of the efficiency gradient $|\nabla|\mathbf{B}_1^+||\sqrt{P_a}[\mu T/m/\sqrt{W}]$ obtained by the SWGA coil with a head model in Figure 7 using A, "standard" and B, optimized excitations

efficiency over the TEM coil, while providing practically the same relative (magnetic) field distribution in the head model phantom. However, the stronger RF magnetic field caused a stronger RF electric field as well in this case, so the electric field distribution, and thus the specific absorption rate (SAR), is in favor of the microstrip array, with the maximum field strength in the model being about 60% of that with the SWGA array.

Observing the transmit efficiencies given in Table 1, we can conclude that the SWGA exciter proposed in this work yields higher efficiencies than all those reported in the literature. Note that most reported results in the literature include relative field maps, SNR, or alternative quantities which are not suitable for comparison with absolute efficiencies reported here.

It can be seen from Figure 10 that RF shimming of the SWGA coil, with the head model, can indeed significantly improve the field uniformity in the imaged subject. In addition, the optimization yields an improvement of 35.4% in the standard deviation of the computed efficiency, which is on a par with results reported in ref. 34. Of course, optimized field uniformity results in reduced overall efficiency, which is again consistent with all reported RF shimming experiments.[32-36]

5 | CONCLUSIONS

This article has proposed a novel RF coil for ultra-high field MRI in the form of a multi-channel SWGA. To further improve the efficiency of the exciter, we have proposed adding a low-loss high-permittivity dielectric on each of the slotted waveguides, which performs as a basic lens. We have presented a comprehensive CEM numerical study, along with basic RF measurements, to characterize the SWGA RF coil at 7T. The study shows that the proposed arrays can efficiently generate circularly polarized magnetic fields, highly desirable for good quality imaging. Some of the other characteristics of the new coil are good field uniformity, negligible axial z-component of the RF magnetic field, arbitrary large FOV, and excellent transmit efficiency, with and without the dielectric lenses. The observed transmit efficiency of the array in the human head simulation experiment is over 2 $\mu T/\sqrt{W}$, whereas it is lower than 0.5 $\mu T/\sqrt{W}$ in all results reported in the literature. Moreover, by our own simulations of both structures, the SWGA coil yields a 130% improvement in the computed efficiency over the state-of-the-art microstrip TEM array coil, while providing practically the same relative field distribution, but higher SAR levels, in the head model

phantom. The measured isolation between elements in the SWGA is 33 dB or higher, and such an excellent isolation and low coupling enables a strong basis for parallel imaging. The capability of the SWGA coil for effective RF shimming has been demonstrated in an example of excitation of the 12-tissue human head model phantom in a 7T MRI bore, showing that, even with a rough preliminary optimization technique, RF shimming of the SWGA coil can indeed significantly improve the field uniformity in the imaged subject. To enable proper operation, the waveguide needs to be filled with a low-loss high-permittivity dielectric, to reduce the waveguide dimensions and enable practical coil design.

We remark that the SWGA exciter proposed and described in the examples in this article is subject to further optimizations. Namely, configuration of the slots from Figure 1 can be optimized for the certain environment to yield maximum radiation efficiency without influencing the purity of polarization. In particular, distances l_i, $i = 1, \ldots, N_S$, and the slot angle θ can be varied to achieve the required radiation properties and impedance matching. In addition, if detuning of the antennas is required, it can be done using PIN diodes.[41-43] Finally, the waveguides can be made shorter or longer, incorporating fewer or more slots, depending on the desired FOV. Note that this change does not influence the overall distribution of the magnetic field. It will always remain qualitatively the same, because it is obtained as superposition of fields radiated by the (electrically short) dipoles, that is, waveguide slots, which, in turn, are always fed by perfectly phased standing wave inside the waveguide. In contrast, for instance, increasing the lengths of strips in the microstrip array will result in the change of current distributions along the strips due to increase of their electrical length. This, in turn will result in significant changes in the generated magnetic field.

ACKNOWLEDGMENTS

This work was supported by the National Science Foundation under grant ECCS-1307863 and by the Serbian Ministry of Education, Science, and Technological Development under grant TR-32005.

REFERENCES

1. Haacke EM, Brown RW, Thompson MR, Venkatesan R. *MRI: Physical Principles and Sequence Design*. New York, NY: Willey; 1996.
2. Vaughan JT, Garwood M, Collins CM, et al. 7T vs. 4T: RF power, homogeneity, and signal-to-noise comparison in head images. *Magn Reson Med*. 2001;46:24-30.
3. Hoult DI. Sensitivity and power deposition in a high-field imaging experiment. *J Magn Reson Imaging*. 2000;12:46-67.
4. Kangarlu A, Baertlein BA, Lee R, et al. Dielectric resonance phenomena in ultra high field MRI. *J Comput Assist Tomogr*. 1999;23:821-831.
5. Collins CM, Li S, Smith MB. SAR and B1 field distributions in a heterogeneous human head model within a birdcage coil. *Magn Reson Med*. 1998;40:847-856.
6. Collins CM, Smith MB. Signal-to-noise ratio and absorbed power as functions of main magnetic field strength, and definition of "90°" RF pulse for the head in the birdcage coil. *Magn Reson Med*. 2001;45:684-691.
7. Hoult DI. The principle of reciprocity in signal strength calculations—a mathematical guide. *Concepts Magn Reson*. 2000;12:173-187.
8. Vaughan JT, Adriany G, Snyder CJ, et al. Efficient high-frequency body coil for high-field MRI. *Magn Reson Med*. 2004;52:851-859.
9. Vaughan JT, Snyder CJ, DelaBarre LJ, et al. Whole-body imaging at 7T: Preliminary results. *Magn Reson Med*. 2009;61:244-248.
10. Adriany G, Van de Moortele P-F, Wiesinger F, et al. Transmit and receive transmission line arrays for 7 Tesla parallel imaging. *Magn Reson Med*. 2005;53:434-445.
11. Katscher U, Börnert P, Leussler C, van den Brink JS. Transmit SENSE. *Magn Reson Med*. 2003;49:144-150.
12. Zhu Y. Parallel excitation with an array of transmit coils. *Magn Reson Med*. 2004;51:775-784.
13. Setsompop K, Wald LL, Alagappan V, et al. Parallel RF transmission with eight channels at 3 Tesla. *Magn Reson Med*. 2006;56:1163-1171.
14. Hetherington HP, Avdievich NI, Kuznetsov AM, Pan JW. RF shimming for spectroscopic localization in the human brain at 7 T. *Magn Reson Med*. 2010;63:9-19.
15. Setsompop K, Alagappan V, Gagoski B, et al. Slice-selective RF pulses for in vivo B 1+ inhomogeneity mitigation at 7 tesla using parallel RF excitation with a 16-element coil. *Magn Reson Med*. 2008;60:1422-1432.
16. Metzger GJ, Snyder C, Akgun C, Vaughan T, Ugurbil K, Van de Moortele P-F. Local B1+ shimming for prostate imaging with transceiver arrays at 7T based on subject-dependent transmit phase measurements. *Magn Reson Med*. 2008;59:396-409.
17. Van de Moortele P-F, Akgun C, Adriany G, et al. B1 destructive interferences and spatial phase patterns at 7 T with a head transceiver array coil. *Magn Reson Med*. 2005;54:1503-1518.
18. Wu B, Wang C, Kelley DAC, et al. Shielded microstrip array for 7T human MR imaging. *IEEE Trans Med Imaging*. 2010;29:179-184.
19. Webb AG, Van de Moortele PF. The technological future of 7 T MRI hardware. *NMR Biomed*. 2016;29:1305-1315.
20. Vaughan T, DelaBarre L, Snyder C, et al. 9.4T human MRI: preliminary results. *Magn Reson Med*. 2006;56:1274-1282.
21. Metzger GJ, van de Moortele P-F, Akgun C, et al. Performance of external and internal coil configurations for prostate investigations at 7 T. *Magn Reson Med*. 2010;64:1625-1639.
22. Metzger GJ, Auerbach EJ, Akgun C, et al. Dynamically applied B1+ shimming solutions for non-contrast enhanced renal angiography at 7.0 tesla. *Magn Reson Med*. 2013;69:114-126.
23. Raaijmakers AJE, Luijten PR, van den Berg CAT. Dipole antennas for ultrahigh-field body imaging: a comparison with loop coils. *NMR Biomed*. 2016;29:1122-1130.

24. Leussler C, Wirtz D, Vernickel P. Slot-line antenna array for high field parallel transmit MRI. *Proc Int Soc Magn Reson Med*. 2010;18:3828.
25. ANSYS HFSS v.17.0.0. 2016. www.ansys.com/products/electronics/ansys-hfss. Accessed November 15, 2017.
26. Notaros BM. *Electromagnetics*. Upper Saddle River, NJ: Pearson Prentice Hall; 2010:840 pp.
27. Balanis CA. *Modern Antenna Handbook*. Hoboken, NJ: Wiley; 2008.
28. Jin J-M. *Theory and Computation of Electromagnetic Fields*. Hoboken, NJ: Wiley; 2010.
29. Enjiu RK, Perotoni MB. Slotted waveguide antenna design using 3D EM simulation. *Microwave J*. 2013;56:72-84.
30. Andreychenko A, Kroeze H, Boer VO, Lagendijk JJW, Luijten PR, van den Berg CAT. Improved steering of the RF field of traveling wave MR with a multimode, coaxial waveguide. *Magn Reson Med*. 2013;71:1641-1649.
31. Andreychenko A, Kroeze H, Klomp DWJ, Lagendijk JJW, Luijten PR, van den Berg CAT. Coaxial waveguide for travelling wave MRI at ultrahigh fields. *Magn Reson Med*. 2012;70:875-884.
32. Mao W, Smith MB, Collins CM. Exploring the limits of RF shimming for high-field MRI of the human head. *Magn Reson Med*. 2006;56:918-922.
33. Avdievich NI, Oh S, Hetherington HP, Collins CM. Improved homogeneity of the transmit field by simultaneous transmission with phased array and volume coil. *J Magn Reson Imaging*. 2010;32:476-481.
34. Ibrahim TS, Lee R, Baertlein BA, Abduljalil AM, Zhu H, Robitaille P-ML. Effect of RF coil excitation on field inhomogeneity at ultra high fields: a field optimized TEM resonator. *Magn Reson Imaging*. 2001;19:1339-1347.
35. Ibrahim TS. Ultrahigh-field MRI whole-slice and localized RF field excitations using the same RF transmit array. *IEEE Trans Med Imaging*. 2006;25:1341-1347.
36. Ibrahim TS, Tang L. Insight into RF power requirements and B1 field homogeneity for human MRI via rigorous FDTD approach. *J Magn Reson Imaging*. 2007;25:1235-1247.
37. Son HW, Cho YK, Gopinath A, Vaughan JT, Lee CH, Yoo H. B1+ shimming with SAR reduction in high-field MRI. *J Electromagnet Wave Appl*. 2013;27:1521-1524.
38. Brunner DO, Paška J, Froehlich J, Pruessmann KP. Traveling-wave RF shimming and parallel MRI. *Magn Reson Med*. 2011;66:290-300.
39. Zhang B, Sodickson DK, Lattanzi R, Duan Q, Stoeckel B, Wiggins GC. Whole body traveling wave magnetic resonance imaging at high field strength: homogeneity, efficiency, and energy deposition as compared with traditional excitation mechanisms. *Magn Reson Med*. 2012;67:1183-1193.
40. Snyder CJ, DelaBarre L, Moeller S, et al. Comparison between eight- and sixteen-channel TEM transceive arrays for body imaging at 7 T. *Magn Reson Med*. 2012;67:954-964.
41. Chen KH, Wu SJ, Kang CH, Chan CK, Tarng JH. A frequency reconfigurable slot antenna using PIN diodes. In: Asia Pacific Microwave Conference, Singapore, 2009;1930-1933.
42. Lin YY, Liao CL, Hsieh TH, Liao WJ. A novel beam-switching array antenna using series-fed slots with PIN diodes. *IEEE Antennas Wirel Propag Lett*. 2017;16:1393-1396.
43. Sarrazin J, Mahe Y, Avrillon S, Toutain S. Pattern reconfigurable cubic antenna. *IEEE Trans Antennas Propag*. 2009;57:310-317.

How to cite this article: Ilić MM, Notaroš BM. Slotted-waveguide array radio frequency coil for ultra-high-field magnetic resonance imaging. *Concepts Magn Reson Part B*. 2018;48B:e21367. https://doi.org/10.1002/cmr.b.21367